Journal of Sound and Vibration 640 (2026) 119907

Contents lists available at ScienceDirect

Journal of Sound and Vibration

journal homepage: www.elsevier.com/locate/jsvi

Influences of internal stress in the dynamic behavior of integrated photonic ultrasound transducers

Sabiju Valiya Valappil [a,*], Martin Verweij [a], Peter Harmsma [b], Maurits van der Heiden [c], Paul van Neer [c]

[a] Faculty of Applied Sciences, Delft University of Technology, Lorentzweg 1, Delft, 2628 CJ, The Netherlands
[b] Nederlandse Organisatie voor Toegepast Natuurwetenschappelijk Onderzoek (TNO), Stieltjesweg 1, Delft, 2628CK, Netherlands
[c] Nederlandse Organisatie voor Toegepast Natuurwetenschappelijk Onderzoek (TNO), Oude Waalsdorperweg 63, Den Haag, 2509JG, Netherlands

ARTICLE INFO

Keywords:
Photonic ultrasound transducers
Residual stress from fabrication
Dynamic response
Post-buckling behavior
Plate vibration
Numerical modeling

ABSTRACT

Integrated photonic ultrasound transducers (IPUTs) are compact, high-sensitivity devices that combine mechanical sensing with optical readout using integrated photonics. IPUTs typically consist of optical waveguides integrated on a thin mechanical plate that serves as the acoustic sensing element. In many realizations, this plate is formed from thermally oxidized silicon dioxide layers commonly used in photonic fabrication processes. The oxidation process introduces significant residual compressive stress–typically between 200 MPa and 400 MPa–as the structure cools to room temperature. Such stresses can strongly influence the dynamic response of the plate through their contribution to the geometric stiffness of the structure. In this work, the influence of internal stress on the resonance frequency and receive transfer function (RTF) of IPUTs is investigated. Finite element models incorporating residual stress and geometric nonlinearity are developed and validated against experimental measurements and results reported in the literature. Parametric analysis shows that increasing compressive stress progressively reduces the resonance frequency while enhancing the RTF as the structure approaches the critical buckling condition. Beyond this point, changes in the prestressed equilibrium configuration lead to transitions in the dominant vibration mode, producing abrupt variations in the resonance frequency and RTF. These results highlight the importance of accounting for residual stress in the design and analysis of IPUTs and similar plate-based acoustic sensors to ensure reliable dynamic performance and predictable sensitivity.

1. Introduction

Ultrasound transducers (UTs) are widely used in diverse domains, including nondestructive evaluation [1], medical diagnostics [2], flow measurement [3], distance measurement [4], and food processing [5], among others. The global market for UTs is expected to reach US$9.3 billion in 2027 [6,7]. Conventional UTs typically exploit the piezoelectric effect [8], where acoustic-to-electrical energy conversion depends on the properties of piezoelectric ceramics such as lead zirconate titanate. Although considered hazardous, these materials are still dominating the transducer market, as lead-free substances show inferior electromechanical properties [9]. Alternative technologies such as microelectromechanical systems (MEMS)-based piezoelectric micromachined ultrasound transducers

* Corresponding author.
E-mail addresses: S.ValiyaValappil@tudelft.nl (S.V. Valappil), M.D.Verweij@tudelft.nl (M. Verweij), peter.harmsma@tno.nl (P. Harmsma), maurits.vanderheiden@tno.nl (M. van der Heiden), paul.vanneer@tno.nl (P. van Neer).

https://doi.org/10.1016/j.jsv.2026.119907
Received 22 October 2025; Received in revised form 21 May 2026; Accepted 22 May 2026
Available online 25 May 2026

(pMUTs) [10] and capacitive micromachined ultrasound transducers (cMUTs) [11] have been introduced to address size, integration, and cost constraints, particularly in high-volume applications. pMUTs use thin-film piezoelectric layers to deform the membrane/plate and to convert the deformation to electric signals, while cMUTs rely on electrostatic forces for actuating/sensing.

Integrated photonic ultrasound transducers (IPUTs) are an emerging class of devices that combine acoustic sensing with optical interrogation systems, thus separating the sensing and read-out portions [12]. IPUTs are optomechanical devices where the vibration of a mechanical resonator (due to the incoming acoustic pulse) modulates the properties of the optical circuit. IPUTs, pMUTs, and cMUTs are generally fabricated via microfabrication technology (semiconductor manufacturing, e,g, complementary metal-oxide semiconductor (CMOS)) where oxide/nitride layers are used as insulators [13]. The resonator portions of IPUTs are composed solely of insulator layers [14]. These insulator layers are generally formed (grown or deposited) by thermal oxidation, chemical vapor deposition, physical vapor deposition, or epitaxy [13]. Among these, thermal oxidation is commonly adopted because of the high surface finish, geometric accuracy, and optical quality [15].

The oxidation process occurs at elevated temperatures (900°C to 1200°C) [16]; thus, the oxide layers experience substantial internal compressive stresses (residual stress) when cooled to room temperature for operation. These stress levels can range from 200 MPa to 400 MPa on average [17] and go up to 1 GPa [18]. In cMUTs and pMUTs, other adjacent stress-free layers (applied after fabrication) induce a resulting tensile or compressive stress [19]. In contrast, in IPUTs, the membranes/plates are not in contact with additional structures other than optical waveguides, which are generally insignificant in size compared to the membrane, and hence the internal stress is always compressive, unless additional tensile layers are applied, and can influence the IPUT's dynamic response greatly.

The internal stress influences the strength and stability of the MEMS device and can cause fracture, delamination, and microstructural changes in the material [20]. Furthermore, in cMUTs the internal stress modifies the stiffness, collapse voltage, resonance frequency, transformer ratio, coupling coefficient, and bandwidth [21,22]. Thus, Xu et al., developed a model based on the finite element method (FEM) to study the influence of internal stress on the cMUT's response. They found that internal tensile stress benefits the collapse voltage, sensitivity, and output pressure, while internal compressive stress improves stiffness, transformer ratio, and output voltage [22]. In addition, internal stress also influences the dynamic behavior of the cMUT, as studied by Walter et al., where a variation in the resonance frequency is observed due to internal tensile stress [23]. Similarly, in the case of pMUTs, the internal stress alters the resonance frequency [24]. Dangi and Pratap proposed a system-level approach for designing a pMUT with a multilayer circular plate having residual tensile stress, where the variation in resonant frequency with respect to internal stress is determined [25].

The influences of internal stress on the performance of IPUTs have also been extensively investigated [26–31]. Zhang et al. obtained a cavity-optomechanical transducer with a high resonance frequency and quality (Q) factor by tuning the stresses in the clamps to be three times the residual internal stress [29]. Rochus et al. proposed an analytical model to study a Mach-Zehnder interferometer (MZI)-based micro-optomechanical pressure sensor having internal stress and found a close match with experiments [26,28]. Westerveld et al., numerically modeled the behavior of optomechanical ultrasound sensors using FEM and photonic circuit equations in which internal stresses were included [27]. They found that the resonance frequency of the device is highly affected by internal stress. However, to the best of our knowledge, no studies investigate the influence of variations of internal stress in the dynamic response of IPUTs, including the effects of higher vibrational modes due to the plate's post-buckling behavior.

In this work, we develop a numerical model based on FEM to study the influences of internal stress on IPUTs' dynamic response. We validate the model by comparing it to the results from the literature and our experiments. We further use the model to perform parametric studies to determine IPUTs' behavior for a wide range of internal stress values. This allows us to utilize internal stress as a design variable to optimize the IPUT's performance.

2. Problem description

2.1. Internal stress development in a silicon oxide layer

A film of SiO_2 is grown on the silicon substrate by oxidation either with dry oxygen or water (See Fig. 1). Although dry oxygen results in a denser interface with better interface properties, the oxidation rate is higher with water and water-based oxidation is therefore used for films thicker than 0.2 μm [32]. As mentioned in the introduction, the oxidation process is generally performed in a furnace with temperatures ranging from 900°C to 1200°C. Cooling down from this high temperature to room temperature leads to the generation of thermal stresses along the interface of the substrate (Si) and the oxide, which is dependent on the thermal expansion coefficients of both materials. Thermal stress (σ_t) can be calculated via the following expression [33]:

$$\sigma_t = \frac{E_f\left(\alpha_s - \alpha_f\right)\Delta T}{\left(1 - \nu_f\right)}, \tag{1}$$

where E_f, ν_f, and α_f are, respectively, the elastic modulus, the Poisson's ratio, and the thermal expansion coefficient of the film material, which is SiO_2. α_s is the thermal expansion coefficient of the substrate (Si) while $\Delta T = T_{\text{room}} - T_{\text{process}}$ is the temperature difference between operation (room temperature) and fabrication (process temperature), which is negative, hence the thermal stress σ_t is compressive. α_s has been determined for a wide temperature range in the literature, which at room temperature is about $2.6 \times 10^{-6}\,\text{K}^{-1}$, at 1162.5 K (890°C) about $4.27 \times 10^{-6}\,\text{K}^{-1}$ and at 1513.2 K (1240°C) around $4.76 \times 10^{-6}\,\text{K}^{-1}$ [34]. The coefficient of thermal expansion for SiO_2 is temperature-independent and approximately equals to $0.56 \times 10^{-6}\,\text{K}^{-1}$ [35]. Using these coefficients, elastic moduli, and temperature range, the thermal stress can be determined, which is found in the literature to be in the range of 200 MPa to 400 MPa [36]. Since Si wafers are generally circular in nature, it is more convenient to study the stresses developed in

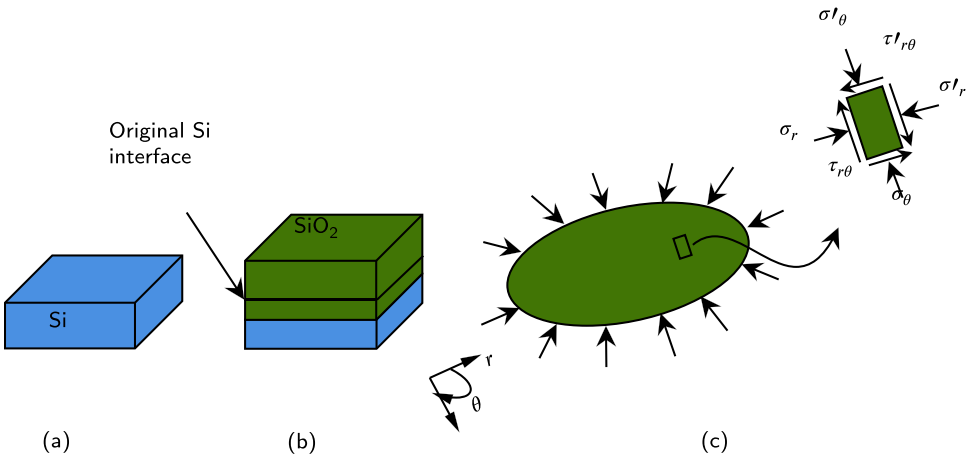

Fig. 1. Schematic representation of the (a) Si substrate where (b) SiO_2 is grown by thermal oxidation, and (c) SiO_2 layer having uniform internal stress with a small strip showing a free body diagram with components of the stress tensor in polar coordinates.

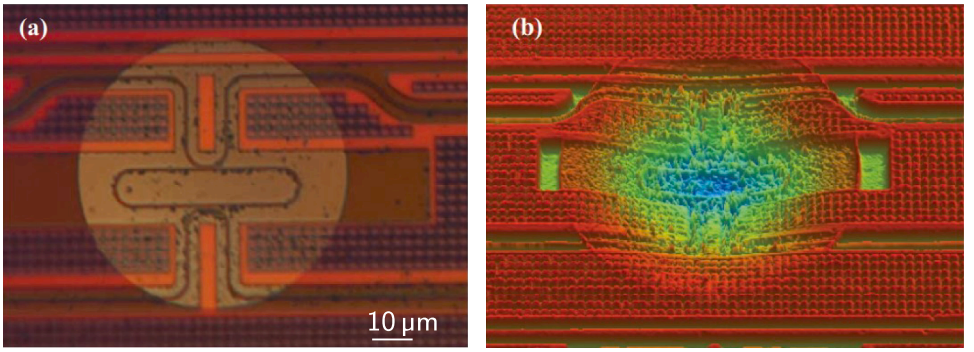

Fig. 2. Fabricated IPUT device. (a) Optical microscope image of RR-based IPUT based on SOI-on Si platform, (b) white-light interferometry showing buckling of the SiO_2 plate [27].

the deposited oxide layer in polar coordinates, as shown in Fig. 1(c). The compressive stress operating on the oxide layer can be represented as a stress tensor with σ_r (radial component) and σ_θ (angular component). $\tau_{r\theta}$ is the shear stress developed in the layer. As the oxide layers are thin (up to a few µm compared to the substrate with thickness of several hundreds of µm), the influence of stress in the axial direction σ_z (perpendicular to the $r-\theta$ plane) will be negligible and can be ignored. Induced internal stresses may adversely affect the SiO_2 layer and can cause several failure phenomena such as plastic deformation, delamination, and buckling [36].

2.2. Buckling in IPUTs due to internal stress

The high residual stress developed due to the thermal oxidation process can lead to buckling of the SiO_2 plate in IPUT devices, as shown in Fig. 2(b) from [27]. The device used here is an IPUT based on a SOI wafer and a ring resonator (RR) read-out, where the plate has a diameter 120 µm and thickness 2.5 µm (see Fig. 2(a)). The buckled plate exhibits a buckling mode similar to the schematic from Fig. 3(b). Now, we investigate in detail the buckling of plate-like structures.

2.3. Plate buckling and critical loads

Buckling is the sudden change in the geometry of the structure (for example, a bar or plate) under a compressive load. In the case of a thin plate, the buckling occurs when the compressive load exceeds the critical load, whose magnitude can be much lower than the failure load. Unlike in the case of columns, where the buckled members are non-functional, a buckled plate is still stable and can operate nominally [37].

Fig. 3(a) shows the fundamental buckling mode of a clamped circular plate. The critical buckling load (σ_c) can be calculated using the following expression [38]:

$$\sigma_c = \frac{kE\left(\frac{2t_p}{D}\right)^2}{\left(1-\nu^2\right)}, \tag{2}$$

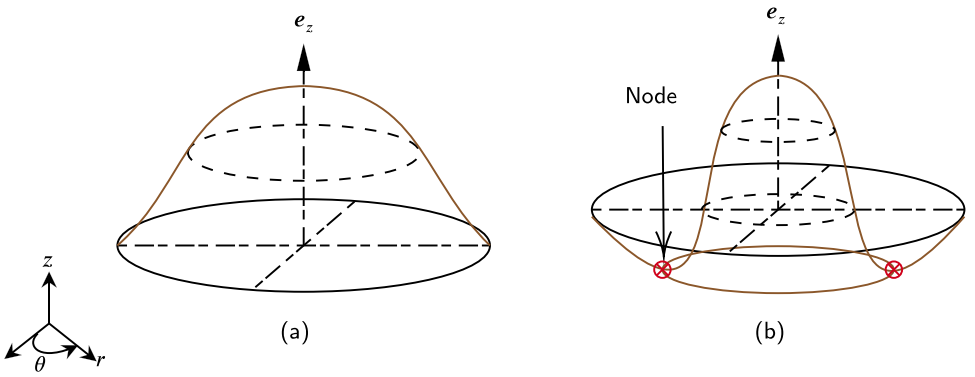

Fig. 3. Schematic representation of the (a) first and (b) second buckling modes of a clamped circular plate. The solid black ellipses show the undeformed (initial) shape, while the brown curves in both figures capture the edges of the buckled plate. The node in the second mode is marked using red crosses in (b). (For interpretation of the references to colour in this figure legend, the reader is referred to the web version of this article.)

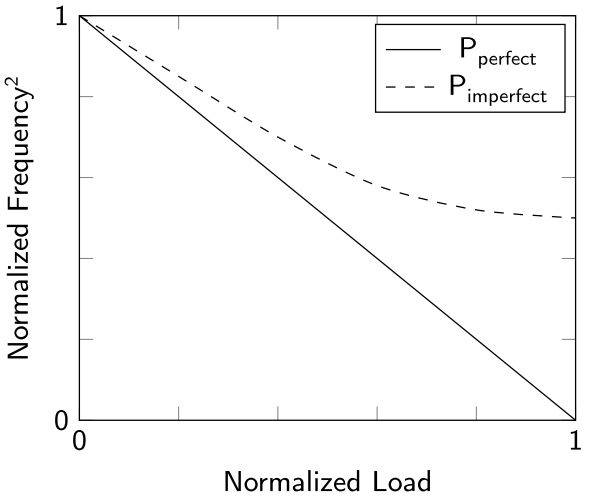

Fig. 4. Conceptual representation of frequency^2 vs load for perfect (solid) and imperfect (dashed) plates. At the critical buckling load the perfect plate loses stability and the resonance frequency reaches zero, while due to imperfections, the resonance frequency follows a post-buckling path (without reaching zero) in the case of an imperfect plate.

where k is the buckling coefficient, which is a non-dimensional parameter depending on the aspect ratio and the boundary conditions, E is the elastic modulus, D is the diameter, t_p is the thickness of the plate, and ν is Poisson's ratio. Noteworthy, the above Eq. (2) only holds for the fundamental buckled condition, although the plate possesses multiple buckling modes. Fig. 3(b) shows the secondary buckling mode, which has a node (marked with red crosses). The presence of the node flips the sign of displacement across it and can lead to more complicated dynamics, as will be discussed later.

2.3.1. Buckling bifurcation and imperfection sensitivity

When a plate is subjected to in-plane compressive stress, the effective bending stiffness governing its transverse vibration decreases due to the geometric stiffness associated with the prestress field. As a result, the natural frequencies of the structure reduce progressively as the compressive load increases [38]. For a perfectly flat plate, classical stability theory predicts that the square of the natural frequency decreases approximately linearly with increasing compressive load and approaches zero at the critical buckling load, where a bifurcation occurs as shown using a solid line in Fig. 4. In practical structures, however, small geometric imperfections or residual stresses smooth out this bifurcation, resulting in a continuous nonlinear variation of the vibration frequency with load (see the dashed curve in the same figure). This framework provides a qualitative reference for interpreting the stress-dependent frequency behavior.

2.4. Linear buckling analysis (eigenvalue formulation)

To assess the instability of the plate and obtain higher buckling modes, a linear buckling analysis is performed numerically [39]. This analysis provides the critical stress levels and associated mode shapes where the undeformed plate loses stability. Within the

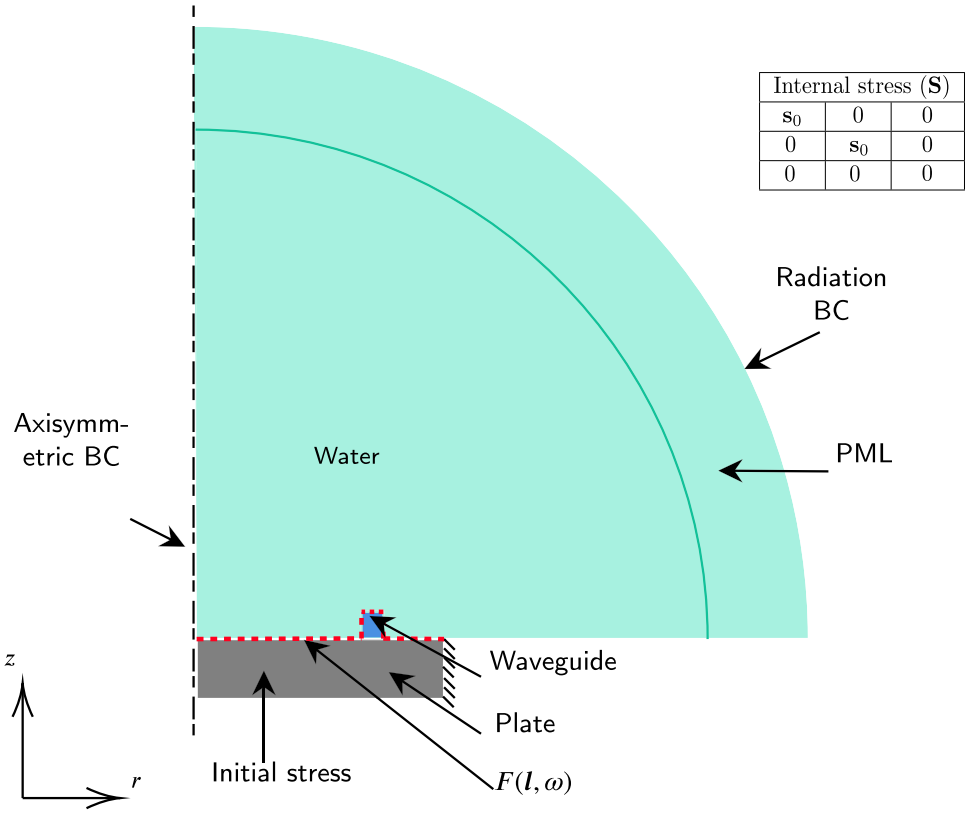

Fig. 5. Schematic representation of the dynamic finite element model of an IPUT with internal stresses applied to the plate portion. The IPUT is assumed to be axisymmetric, while a perfectly matched layer and acoustic radiation boundary condition (BC) ensure a reflection-free analysis. Although the waveguide shown here is a single ring, it can have multiple loops in the case of an MZI (see Section 3.2 for details). A frequency-dependent prescribed boundary load is applied on the top surface of the IPUT. The table shows the tensor representation of the compressive internal stress.

finite element framework, the discretized equilibrium of the plate (or any structure) in the presence of an in-plane stress field can be expressed as

$$\left(\mathbf{K} + \alpha_{cr}\mathbf{K}_{\sigma}\right)\phi = 0, \tag{3}$$

where $\mathbf{K}$ is the linear stiffness matrix, $\mathbf{K}_{\sigma}$ is the geometric stiffness associated with the in-plane stress state, α_{cr} is the load factor (eigenvalue), and ϕ is the buckling mode shape (eigenvector). $\mathbf{K}_{\sigma}$ represents the contribution of plate stresses to the structural stiffness of the plate and depends on the prescribed in-plane stress distribution. Its explicit formulation, consistent with the nonlinear kinematics adopted in this work, is introduced in Section 2.5.2.

The eigenvalue problem yields a set of critical load factors $\alpha_{cr,i}$, from which the critical stresses $\sigma_{cr,i}$ are obtained. The lowest eigenvalue defines the first bifurcation point, at which the fundamental stiffness of the structure vanishes and the flat equilibrium configuration becomes unstable. Similarly, higher eigenvalues correspond to higher-order bifurcation modes. As compressive stress increases, the effective stiffness decreases, causing the fundamental natural frequency to approach zero at the critical condition. Noteworthy, this analysis is performed about the undeformed configuration and therefore only identifies bifurcation loads and mode shapes. The post-buckling behavior is not captured and is instead addressed through the geometrically nonlinear formulation introduced in the following section.

The computed critical loads are used as reference points to interpret the prestress-dependent dynamic response later in the results section, particularly the changes in the natural frequency and mode shapes across stability regions.

2.5. Analysis of internal stress in IPUTs using FEM

2.5.1. Wave propagation through IPUTs

Since our IPUT is designed to operate in a fluid medium (e.g., water), the interaction of waves in both solid and fluid media is present. Fig. 5 shows the schematic of the axisymmetric model of an IPUT operating in water. The wave propagation in the solid domain is governed by the elastic wave equation, in the absence of losses, and an external source term, which takes the form [40],

$$\rho_s \ddot{\mathbf{u}} = \nabla \cdot \boldsymbol{\sigma}, \tag{4}$$

where $\ddot{\mathbf{u}}$ is the particle acceleration, while ρ_s represents the density of the solid. $\boldsymbol{\sigma}$ is the Cauchy stress tensor in the solid material, whereas $\nabla\cdot$ is the vector divergence operator. For small perturbations (linear behavior), the stresses and strains within the solid domains are related by the following constitutive equation,

$$\boldsymbol{\sigma} = \mathbf{C} : \boldsymbol{\gamma}, \tag{5}$$

where $\boldsymbol{\gamma}$ is the strain tensor (both $\boldsymbol{\sigma}$ and $\boldsymbol{\gamma}$ are rank 2), while $\mathbf{C}$ is the rank 4 elasticity tensor.

The wave propagation through the fluid medium can be represented by the acoustic wave equation that takes the form [41]

$$\nabla^2 p = \rho_f \kappa \ddot{p}, \qquad \nabla^2 \mathbf{v} = \rho_f \kappa \ddot{\mathbf{v}}, \tag{6}$$

where $p(\mathbf{r}, t)$ and $\mathbf{v}(\mathbf{r}, t)$, respectively, represent the acoustic pressure and velocity fields at the spatial coordinate $\mathbf{r}$ and time t. κ is the compressibility of the fluid, ρ_f is its mass density, and ∇^2 is the Laplacian. Since field variables are different in fluid and solid (IPUT) domains, we couple them using a kinematic interface condition, which ensures the continuity of normal velocity across the interface as follows,

$$\mathbf{n}\cdot\nabla p = -\rho_f \mathbf{n}\cdot\ddot{\mathbf{u}}, \tag{7}$$

where ∇ is the gradient operator and $\mathbf{n}$ is the unit outward normal vector along the interface. Additionally, we need a dynamic interface condition to ensure the continuity of traction,

$$-p\mathbf{n} = \mu_s \frac{\partial \mathbf{u}}{\partial \mathbf{n}} + (\lambda_s + \mu_s)(\nabla\cdot\mathbf{u})\mathbf{n}, \tag{8}$$

where λ_s and μ_s are the Lamé coefficients and $\mathbf{u}$ is the particle displacement in the solid domain. The details of these interface conditions can be found in [42]. To solve this boundary value problem (BVP), it still needs the necessary boundary conditions (BCs). We provide a Dirichlet BC (zero displacement) along the outer edge of the plate since it is clamped and a Neumann BC (prescribed force) along the top boundary of the IPUT as marked using a red dashed line in Fig. 5, which takes the following form:

$$F(\mathbf{l}, \omega) = \bar{F} e^{\mathrm{i}\omega t}, \quad \text{applied at} \quad \underline{r} = \underline{l}, \tag{9}$$

where $\bar{F}$ is the constant force amplitude applied along the location $\mathbf{l}$ and $\omega = 2\pi f$ is the angular frequency in rad/s. We use Comsol to solve this dynamic problem via FEM. We employ the solid mechanics interface for the IPUT domain while using the pressure acoustic frequency domain interface for the fluid portion. The solid-fluid interface is modeled via fluid-structure interactions. In practice, the water domain is substantially larger than the IPUT. To mimic this effect, we provide a perfectly matching layer and a plane wave radiation BC on the outer fluid boundary, as shown in the same figure.

2.5.2. Introduction of internal stress into the plate

The internal stress acts as a body force deforming the IPUT in a static setting. Since the aforementioned frequency-domain dynamic analysis operates on the new deformed geometry, the nonlinear influences cannot be ignored. These can be captured by enabling the geometric-nonlinearity option in the Comsol solver settings. This has several consequences for the analysis. Firstly, instead of the engineering strain ($\boldsymbol{\gamma}$), Green-Lagrange strain (GLS – $\boldsymbol{\epsilon}$) is used [43]. This adds higher-order terms to the strain tensor. The normal strain component in the radial direction can be written as follows:

$$\epsilon_r = \frac{\partial u}{\partial r} + \frac{1}{2}\left[\left(\frac{\partial u}{\partial r}\right)^2 + \left(\frac{\partial v}{\partial r}\right)^2 + \left(\frac{\partial w}{\partial r}\right)^2\right], \tag{10}$$

Similarly, the shear strain in the $r-\theta$ plane can be written as:

$$\epsilon_{r,\theta} = \frac{1}{2}\left[\frac{1}{r}\frac{\partial u}{\partial \theta} + \frac{\partial v}{\partial r} - \frac{u}{r} + \frac{1}{r}\frac{\partial u}{\partial r}\frac{\partial u}{\partial \theta} + \frac{1}{r}\frac{\partial v}{\partial r}\frac{\partial v}{\partial \theta} + \frac{1}{r}\frac{\partial w}{\partial r}\frac{\partial w}{\partial \theta} + \frac{w}{r}\frac{\partial v}{\partial r} - \frac{v}{r}\frac{\partial u}{\partial r}\right]. \tag{11}$$

GLS can handle finite rotations, i.e., by using GLS, we can avoid stress artifacts that arise from using engineering strain for large rotation systems. Additionally, the cross-terms present in the strain components allow for coupling between the in-plane and transverse loading (such as in the present case). This has serious implications since the addition of compressive in-plane load modifies the effective stiffness (tangent stiffness) and thereby the dynamic response of the IPUT. Secondly, instead of Cauchy's stress tensor ($\boldsymbol{\sigma}$), the second Piola-Kirchhoff stress tensor ($\mathbf{S}$) is used, which can handle finite deformations [44]. It can be expressed as:

$$\mathbf{S} = J\mathbf{F}^{-1}\cdot\boldsymbol{\sigma}\cdot\mathbf{F}^{-\mathrm{T}}, \tag{12}$$

where J is the Jacobian determinant and $\mathbf{F}$ is the deformation gradient. The internal stress on the SiO_2 layer is applied as shown in the table of Fig. 5. Here, we assume that the loading is uniform and the value of the internal stress $\sigma_r = \sigma_\theta = \sigma_0$ (constant), while also assuming $\sigma_z = \tau_{r\theta} = \tau_{rz} = \tau_{z\theta} = 0$. Using Eqs. (6) to (9) (wave equations, interface, and boundary conditions), we perform a frequency domain analysis of the IPUT. Additionally, by modifying the strain and stress tensors using Eqs. (10)–(12), we perform the IPUT's dynamic analysis with the influence of internal stress. To that end, the geometric nonlinearity in the solver setting is enabled. The nonlinear equilibrium configuration associated with the prescribed internal stress is first computed using a stationary study, after which the dynamic response is obtained through the linearized frequency-domain analysis about this prestressed state. To ensure numerical accuracy, the nonlinear solver is operated with a relative tolerance of 10^{-6}, and mesh refinement studies were conducted to verify convergence of the resonance frequencies.

The numerical analysis provides us with instantaneous values for the pressure, velocity, and displacement. These acoustic and/or elastic parameters are related to the optical domain via the optical length of the waveguide, which is the product of the waveguide

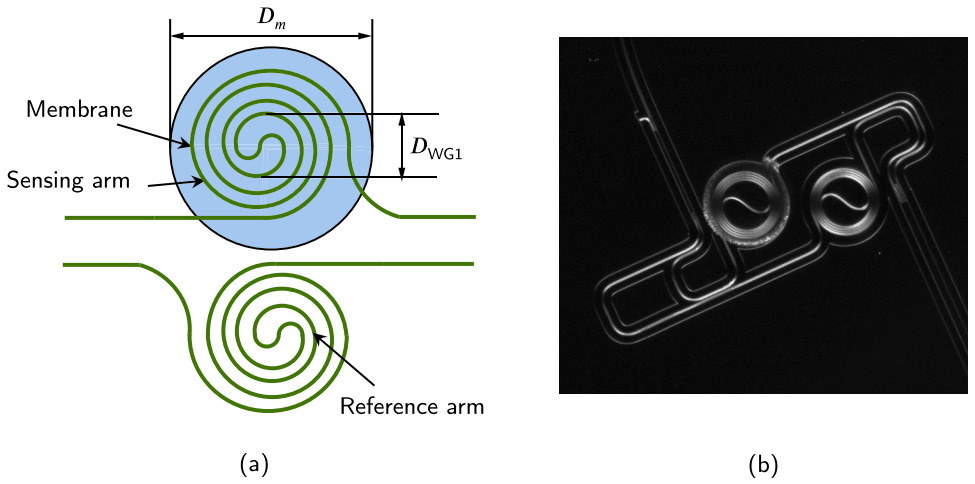

Fig. 6. (a) Schematic representation of the MZI-based IPUT where membrane (blue) and spiral (green) diameters, $D_m = 120\,\mu$m and $D_{WG1} = 60\,\mu$m, respectively, are marked. (b) Photograph of our MZI-based IPUT used in this study. (For interpretation of the references to colour in this figure legend, the reader is referred to the web version of this article.)

physical length and its effective index. The former is directly affected by the plate vibration, while the latter connects the stress induced in the waveguide to the refractive index of the material via the photoelastic tensor. Both influences can be combined in the RTF of a ring resonator based IPUT as described in Equation (18) from our previous article [45], as follows:

$$\left(\frac{\mathrm{d}\lambda}{\mathrm{d}P}\right) = \frac{\lambda}{n_g L}\left(n_{\mathrm{eff}}\frac{\mathrm{d}L}{\mathrm{d}P} + L\frac{\mathrm{d}n_{\mathrm{eff}}}{\mathrm{d}P}\right), \tag{13}$$

where, λ and $\mathrm{d}\lambda$ are, respectively, the optical wavelength of constant round-trip phase and its variation, $\mathrm{d}P$ is the variation in the input pressure, n_{eff} and $\mathrm{d}n_{\mathrm{eff}}$ are the effective index and its variation, respectively, while n_g is the group index. L is the total length of the waveguide, and $\mathrm{d}L$ is its change due to the incoming pressure. We apply the IPUT model with internal stress to two different types of IPUTs. In both cases, the response of the IPUTs is dominated by the mechanical resonant mode, and therefore, the waveguide elongation is the predominant mechanism.

3. Results

To apply the aforementioned IPUT model, we first need to determine the approximate range of internal stress values for the plate. To that end, we extract the internal stress from the fabrication process.

3.1. Internal stress calculation from the thermal oxidation process

We calculate the thermal stress developed in the SiO_2 layer by using Eq. (1) where $E_f = 70\,$GPa and $\nu_f = 0.17$. α_f and α_s were already defined in Section 2.1 (at 900°C, $\alpha_s = 4.27 \times 10^{-6}\,\mathrm{K}^{-1}$ and at 1200°C, $\alpha_s = 4.76 \times 10^{-6}\,\mathrm{K}^{-1}$, and $\alpha_f = 0.56 \times 10^{-6}\,\mathrm{K}^{-1}$). Since the process temperature is from 900°C to 1200°C, we calculate σ_t for both temperature values. At 900°C, $\sigma_t = 282\,$MPa and at 1200°C, $\sigma_t = 416\,$MPa, which agrees with the range from the literature (200 MPa to 400 MPa). As mentioned previously, since these internal stresses are compressive (owing to the negative temperature gradient, i.e., the final value (operating temperature) is lower than the initial value (process temperature)), by sign convention, they are treated as negative values during the analysis stage. We consider two IPUT devices manufactured by different suppliers, both of which use SiO_2 plates as the resonator. The optical circuit of the first device is MZI, whereas for the second one, it is RR.

3.2. Case – 1: Effects of internal stress on a MZI-based IPUT

3.2.1. Geometry and parameters

We use the geometric parameters from Fig. 6 to construct the IPUT model where $D_m = 120\,\mu$m and $D_{WG1} = 60\,\mu$m. In addition, the thickness of the plate $t_m = 2.42\,\mu$m, the width of the waveguide $w_{WG} = 2\,\mu$m, and the thickness $t_{WG} = 3\,\mu$m. Here, the MZI has four loops. From our experiments (published in a previous article [46]), we know that this device has a resonance frequency $f_c = 0.6\,$MHz. We select an internal stress of $\sigma_t = -250\,$MPa (within the range of internal stress values calculated previously, also provided in [46]) to evaluate the dynamic response of the IPUT.

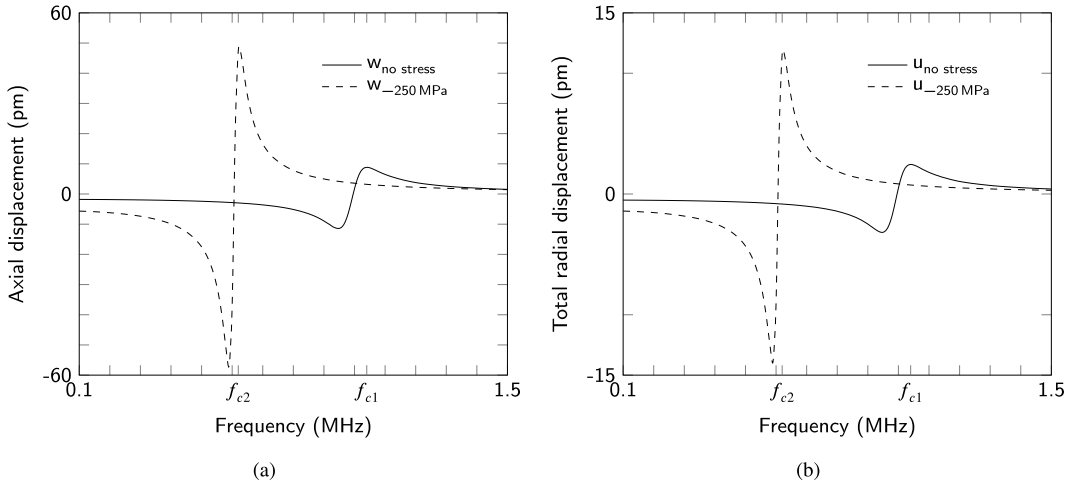

Fig. 7. Comparison of the MZI-based IPUT with and without internal stress (−250 MPa): (a) axial displacement extracted at the center of the plate as a function of frequency where the resonance frequencies $f_{c1} = 1.03$ MHz (without internal stress) and $f_{c2} = 0.62$ MHz (with −250 MPa internal stress), are marked. (b) total radial displacement of all four loops of the MZI as a function of the applied frequency, showing an enhanced radial displacement of the waveguide for −250 MPa internal stress.

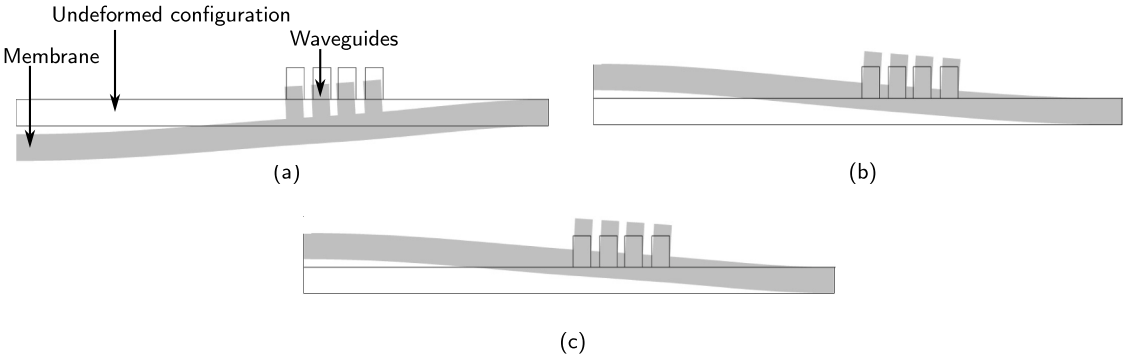

Fig. 8. (a) Displacement profiles of the MZI-based IPUT for different frequencies and internal stresses: (a) 1 Hz and 0 Pa (static deflection) (b) 1.03 MHz and 0 Pa at the first (fundamental) resonant mode, which is similar to the static deflection (with a π phase shift due to the resonance), and (c) 1 Hz and −250 MPa: the static case with internal stress that is again similar to the previous two cases.

3.2.2. Dynamic response of MZI-based IPUT

Fig. 7 compares the dynamic response of the MZI-based IPUT with and without −250 MPa internal stress. The waveguide dimensions are small relative to the plate and thus its stiffness contribution is negligible in first approximation (a few percentage), and therefore the IPUT's dynamics is dominated by the plate. Fig. 7(a) shows the axial displacement of the plate's center as a function of applied frequency. Fig. 7(b) shows the sum of radial displacements of all four loops of the spiral of Fig. 6 as a function of frequency. In the absence of the internal stress, the resonance frequency of the IPUT is $f_{c1} = 1.03$ MHz, which is 69 % higher than the actual experimental value. The model with internal stress predicts the resonance frequency $f_{c2} = 0.62$ MHz, which is much lower than without prestress. This is because the resonance frequency decreases with an increase in internal stress, due to the compressive nature of the internal stress, reducing the effective stiffness. This frequency is very close to the experimental value (less than 2 % deviation). In addition, the axial response shows that the decrease in frequency due to the internal stress also increases the displacement amplitude. This influence is prominent in the IPUT's RTF, which is directly related to the change in total length of the waveguide via its radial displacement as shown in Fig. 7(b). Here, the total radial displacement with the internal stress is 4.8 times higher than the model without the internal stress. The RTF calculated using Eq. (13) for the model without internal stress is 0.1 pm/Pa, while the model with −250 MPa internal stress predicts RTF = 0.495 pm/Pa, which is approximately 5.3 % higher than the experimental results (0.47 pm/Pa from our previous work [46].) Noteworthy, the RTF of the model without internal stress is four times lower than that of the experiment.

Fig. 8 shows the IPUT's axisymmetric displacement for different frequencies and internal stress values. Starting with a case close to a static response Fig. 8(a) shows the behavior for a harmonic load applied at 1 Hz without any internal stress. As expected, the displacement profile is similar to the static deflection of a plate. The IPUT's behavior at its fundamental resonant mode (at 1.03 MHz) without internal stress also resembles the static deflection case as shown in Fig. 8(b), except for the π rad phase difference. The static response with the supplied internal stress (−250 MPa) is shown in Fig. 8(c), which is also similar to the previous two cases. Since all

Table 1
Comparison of buckling analysis with the dynamic response of the MZI-based IPUT where the first three axisymmetric modes are considered. For the same critical load, normalized buckling mode and normalized dynamic mode overlap almost exactly. The displacements are normalized for visualization purposes as seen in the color bar at the bottom. The surface displacement in the first dynamic mode ranges from 0 nm to 0.3 nm, while the second mode from 0 nm to 0.45 nm, and the third mode from 0 nm to 0.022 nm.

Mode	Critical Load σ_{cr} (MPa)	Dominant frequency (MHz)	Normalized buckling mode	Normalized dynamic mode
1	352	0.19	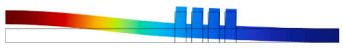	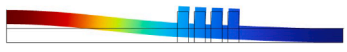
2	567	0.19	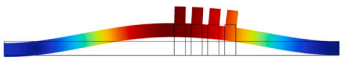	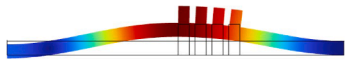
3	1180	0.2	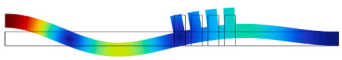	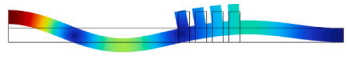
			0	1
				

deformation profiles resemble the fundamental vibration mode, the equilibrium configuration remains close to the flat state and does not exhibit pronounced post-buckling deformation under the applied internal stress.

3.2.3. *Buckling behavior of MZI-based IPUT*

To interpret the observed frequency shift within the framework of elastic stability, a linear buckling analysis is first performed on the undeformed configuration under in-plane compressive stress. This analysis provides the critical loads and associated bifurcation mode shapes, which serve as reference states for the subsequent prestressed vibration analysis.

The lowest eigenvalues that correspond to axisymmetric modes with critical stresses σ_1, σ_2, and σ_3 are shown in Table 1. Asymmetric modes could be present in the 3D analysis, but since the IPUT is axisymmetric, all the analysis are performed with 2D axisymmetric BC. This is also to reduce the computational burden for the nonlinear frequency domain analysis with numerous frequency and internal stress steps. It is noteworthy, the normalized color bar shown here only corresponds to the dynamic modes since the buckling analysis is an eigenvalue analysis where the absolute displacements do not hold any physical meanings. The surface displacement of the first dynamic mode ranges from 0 nm to 0.3 nm, while the second mode is from 0 nm to 0.45 nm, and finally the third mode has the displacement from 0 nm to 0.022 nm. It is emphasized that these critical loads do not imply multiple physical buckling events occurring sequentially in the dynamic response. Rather, they identify admissible bifurcation modes of the perfect structure. In the presence of geometric nonlinearity and unavoidable imperfections, the structure follows a single post-buckling equilibrium path, and the computed resonance frequencies correspond to small-amplitude vibrations about this prestressed configuration. Consequently, the changes in frequency and mode shape are interpreted as transitions in the dominant vibration pattern along the post-buckled equilibrium branch, rather than successive instabilities.

3.2.4. *Parametric response*

To further investigate the influence, we performed a parametric study of the MZI-based IPUT for large range of internal stress values ($\sigma_t = 0$ Pa to $\sigma_t = 1$ GPa), which is still within the limit of thermal stress generated in the oxide layer during fabrication [18]. Furthermore, we also increased the frequency range of the harmonic analysis (ranging from 1 Hz to 9 MHz).

Fig. 9 shows the parametric response of the MZI-based IPUT, where Fig. 9(a) represents the resonance frequency (in MHz) as a function of the applied internal stress. The experimentally obtained resonance frequency (f_c) is also marked in the figure. As mentioned previously, the resonance frequency decreases with an increase in the internal stress. This trend continues until the internal stress reaches the lowest critical buckling load (σ_1), beyond which the flat configuration loses stability and the IPUT vibrates about a post-buckled equilibrium configuration, resulting in sudden changes in the dynamic response. Specifically, as the internal stress increases beyond σ_1, the equilibrium configuration changes from the flat state to a post-buckled configuration, accompanied by a sharp change in the resonance frequency from 0.185 MHz to 2.165 MHz (11.7 times increase). Owing to the stable post-buckling equilibrium of the plate, the IPUT remains operational, and the trend continues as before (i.e., frequency decreases with the increase in the internal stress). To facilitate interpretation, the parametric response is divided into three regimes based on the dominant vibration mode about the prestressed equilibrium configuration. In Zone 1, with σ ranging from 0 Pa to −360 MPa and f ranging from 1.04 MHz to 0.185 MHz, the IPUT vibrates in its fundamental mode, which is shown in Fig. 9(d). In Zone 2, the stress ranges from $\sigma_1 = -370$ MPa to $\sigma_2 = -600$ MPa while the frequency ranges from 2.165 MHz to 0.185 MHz, and the vibration response is dominated by a higher-order

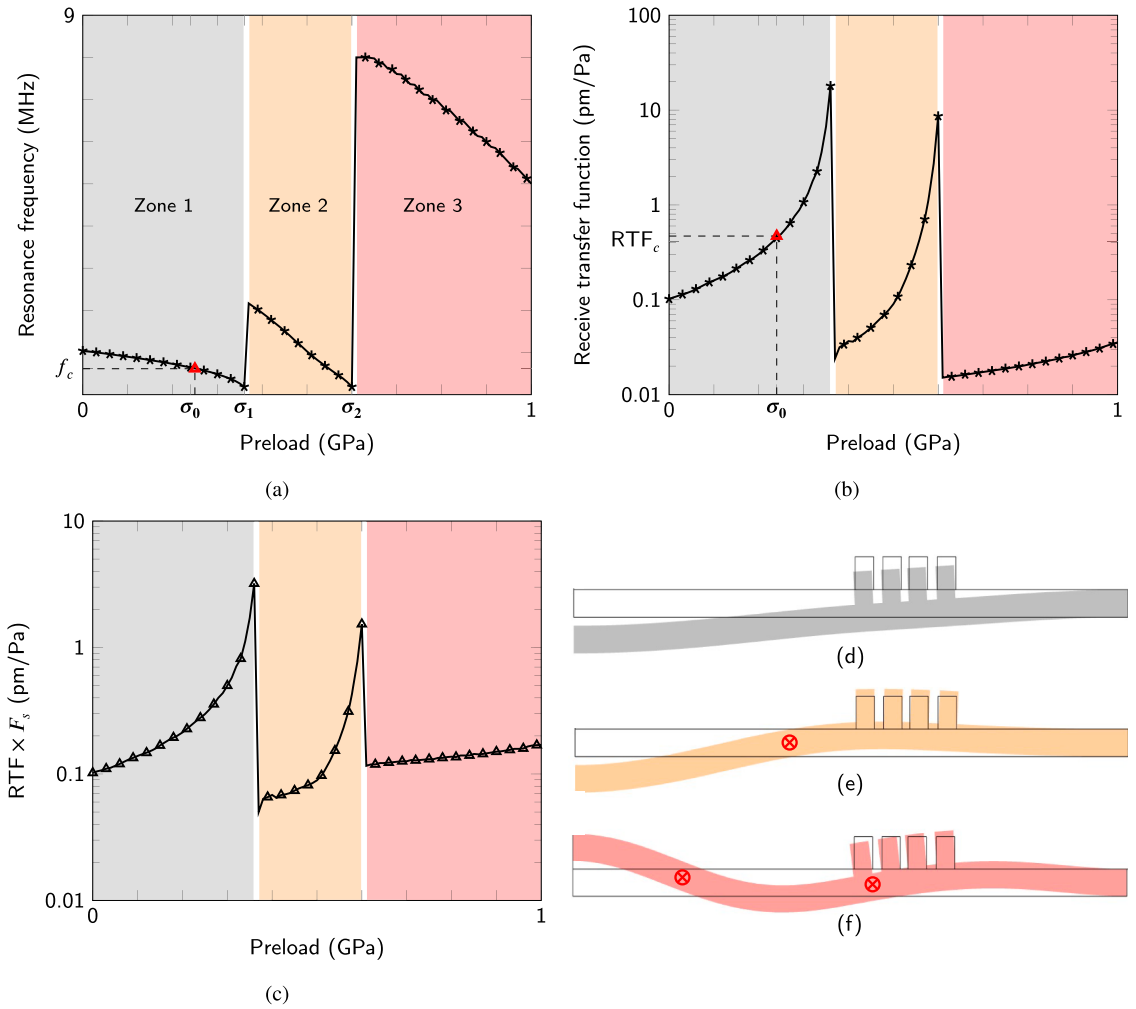

Fig. 9. Parametric response of the MZI-based IPUT: (a) Resonance frequency variation with internal stress from 0 to−1 GPa where the first two buckling loads $\sigma_1 = -360$ MPa and $\sigma_2 = -600$ MPa are marked. The plot is separated into three zones based on the mode shapes of the IPUT. There are sharp discontinuities between each zone, evidence of a mode change. The internal stress experienced by the IPUT ($\sigma_t = -250$ MPa) and the corresponding resonance frequency ($f_c = 0.61$ MHz) obtained experimentally are also marked here. (b) The variation of RTF with the internal stress, where sudden increases in RTF values close to critical loads are visible. The internal stress $\boldsymbol{\sigma}_t$ and corresponding RTF (RTF$_c$ = 0.47 pm/Pa) also attained experimentally are marked in the plot. (c) The variation of the product of RTF with the frequency ratio (F_s) is plotted for the same range of internal stress. (d), (e) and (f), respectively are displacement profiles of the MZI-based IPUT for different frequencies and internal stresses: (d) 0.62 MHz and −250 MPa, i.e., the actual operating condition of the IPUT, which is similar to the resonant mode without internal stress (in Zone 1). (e) 1.93 MHz and −400 MPa, which is the IPUT's behavior after crossing the first critical load (in Zone 2), where its deformation pattern is similar to a second vibration mode with the presence of a node (red cross). (f) 6.86 MHz and −800 MPa operating in Zone 3 after crossing the second critical load, where the IPUT's displacement profile is equivalent to the third vibration mode with two nodes. (For interpretation of the references to colour in this figure legend, the reader is referred to the web version of this article.)

mode shape with a single nodal line as shown in Fig. 9(e) where the location of the node is marked using a red cross, characteristic of vibration about the post-buckled equilibrium configuration. Similarly, in Zone 3 (stresses from 600 MPa to 1 GPa and frequency from 8 MHz to 5 MHz) the vibration response is dominated by a higher-order mode with two nodal lines. Higher vibrational modes, in addition to increasing the resonance frequency, also modify the RTF as shown in Fig. 9(b). Here, the RTF in pm/Pa is represented as a function of the internal stress, where the experimental value (RTF$_c$) is marked. The RTF increases with an increase in internal stress until the vicinity of the lowest critical buckling load, where the transition to a post-buckled equilibrium configuration leads to a sudden change in RTF (18 pm/Pa to 24 fm/Pa, almost three orders of magnitude.) This is much higher than the shift in the resonance frequency (11.7 times) because of the influence of the mode shape in the radial displacements of the waveguides. Beyond the onset of post-buckling, the RTF again follows similar trend with increasing internal stress. It should be emphasized that only the lowest critical buckling load corresponds to a physical loss of stability of the flat configuration; the higher critical stresses indicated in the figure arise from buckling eigenvalue analysis and serve as reference points for interpreting changes in the vibration response, rather

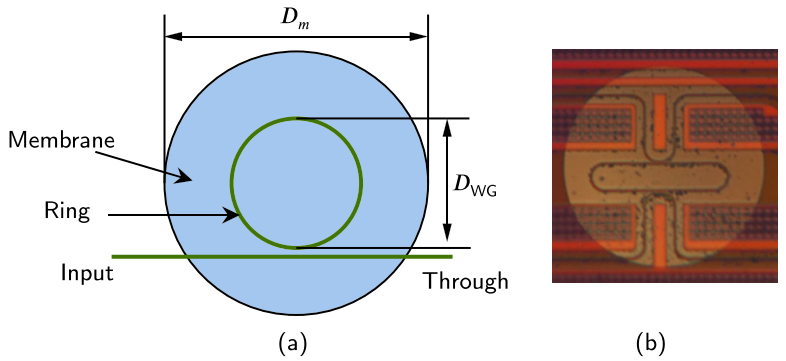

Fig. 10. (a) Schematic representation of the RR-based IPUT where plate and ring diameters are marked. (b) Photograph of an RR-based IPUT from [47].

than representing additional buckling events. The three orders of difference between the RTF values for the same geometry include the influence of frequency, i.e., it takes more energy to drive a system oscillating at a higher frequency than a lower frequency, a decrease or increase in the frequency would directly influence the displacement and thereby the RTF. Therefore, to represent the RTF more realistically, we scale the RTF with a frequency scaling factor fs defined as:

$$F_s = f'/f_0, \tag{14}$$

where f_0 is the resonance frequency in the absence of internal stress and f' is the frequency of interest. The result is shown in Fig. 9(c), where although the trend looks similar to 9(b), the largest variation is 64 times, which is much smaller than 1200 from the RTF plot. Now we proceed to explore the influence of internal stress in an RR-based IPUT.

3.3. Case – 2: Effects of internal stress on an RR-based IPUT

3.3.1. Geometry and parameters

Similarly to the previous case, we construct the RR-based IPUT model with and without internal stress.

The schematic is shown in Fig. 10(a) while a microscopic image is provided in Fig. 10(b). The device is the same as in Fig. 2, for which post-buckling deformation of the plate was reported under residual compressive stress [47]. The geometric parameters are shown in the same figure: $D_m = 124\,\mu$m and $D_{WG} = 36\,\mu$m. In addition, the thickness of the plate $t_m = 2.5\,\mu$m, the width of the waveguide $w_{WG} = 0.44\,\mu$m, and the thickness $t_{WG} = 0.22\,\mu$m. Noteworthy, since the model is axisymmetric, the racetrack RR is assumed to be a circular ring that will influence the IPUT's response, which will be discussed later. From the literature, we know that the resonance frequency of this device is 0.77 MHz [47]. We choose the internal stress to be −425 MPa, which is close to the calculated stress due to thermal oxidation (−416 MPa) in Section 3.1 and perform the dynamic analysis with and without internal stress.

3.3.2. Dynamic response of RR-based IPUT

Fig. 11(a) shows the axial displacement of the plate without internal stress (solid curve) and with −425 MPa internal stress (dashed curve) as a function of the applied frequency, where the resonance frequencies $f_{c1} = 0.62$ MHz (without internal stress – 20 % lower than the experiment) and $f_{c2} = 0.78$ MHz (with internal stress – 1.2 % higher than the experiment) are marked. Unlike MZI-based IPUT, the resonance frequency increases with the internal stress, reflecting vibration about a post-buckled equilibrium configuration rather than a simple reduction in effective stiffness. Furthermore, the response with internal stress also experiences a phase change π. These effects are also visible in the radial displacement plot shown in Fig. 11(b), where, in addition, the peak displacement with the internal stress (2.44 pm) is three times higher than the IPUT without internal stress (0.8 pm). The resulting RTF without internal stress is 0.034 pm/Pa, which is approximately half of the actual RTF (from the literature), while the RTF with internal stress is 0.106 pm/Pa, which is about 60 % higher than the actual value. Note that there is a discrepancy in the ring geometry (race track compared to circle) between the actual device and the model, whose influence is explained in our previous article [45]. In other words, the circular approximation overestimates the radial displacement and thereby the RTF by 33 % compared to the actual racetrack geometry. Correcting for this reduces the RTF (of the internal stressed model) to 0.071 pm/Pa, which is only 8 % higher than the measurement value.

The observed increase in resonance frequency and radial displacement under high compressive stress arises from vibration about a post-buckled equilibrium configuration of the plate, as shown in the displacement profiles in Fig. 12.

Here, the displacement profiles of the almost static response Fig. (12(a)—1 Hz) and the dynamic response Fig. (12(b)—0.62 MHz) without internal stress look similar, while the behavior of IPUT with the prescribed internal stress (−425 MPa) is similar to the second vibration mode with a node (marked with a red cross in Fig. 12(c)). This is due to the change in equilibrium configuration, leading to a vibration mode with a nodal line across which the axial displacement changes sign (from positive to negative, as shown in Fig. 12(c)). Since the radial displacement is directly related to the slope of the axial deflection, its value will be high due to the sign change near the node. Thus, we can observe that the waveguide has experienced a large radial deflection while vibrating at a higher frequency, which has led to an increase in both frequency and RTF.

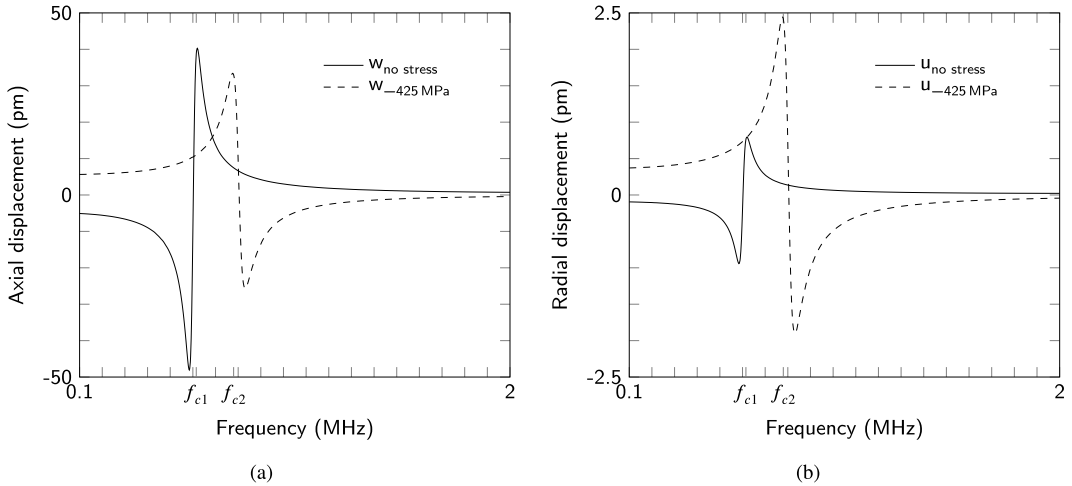

Fig. 11. Comparison of the RR-based IPUT with and without a internal stress (−425 MPa): (a) axial displacement as a function of frequency where the resonance frequencies $f_{c1} = 0.62$ MHz—without internal stress and $f_{c2} = 0.78$ MHz—with −425 MPa internal stress are marked. (b) radial displacement of the ring (of RR) as a function of the applied frequency, showing an enhanced radial displacement of the waveguide with the presence of −425 MPa internal stress. Both axial and radial displacement show that the IPUT with internal stress experiences a π phase shift associated with vibration about a different equilibrium configuration.

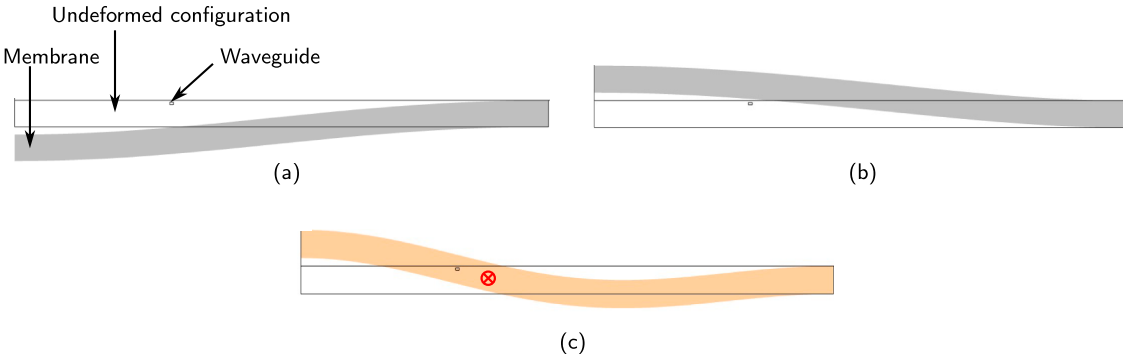

Fig. 12. Displacement profiles of the RR-based IPUT: (a) 1 Hz and 0 Pa equivalent to static deflection, (b) 0.62 MHz and 0 Pa at the first resonant mode, which is similar to the static deflection. (c) 1 Hz and −425 MPa IPUT's static behavior at the prescribed internal stress, which is similar to the second resonant mode of the plate.

3.3.3. Buckling behavior of RR-based IPUT

To provide a consistent interpretation of these results, a linear buckling analysis is conducted for the RR-based IPUT using the undeformed geometry subjected to uniform in-plane compressive stress. The resulting eigenvalue problem yields the critical stresses and corresponding bifurcation modes of the ideal structure. The lowest eigenmodes are found to be axisymmetric, with critical loads σ_1, σ_2, and σ_3 summarized in Table 2.

These bifurcation loads are introduced here as reference quantities and should not be interpreted as indicating multiple sequential buckling events during operation. Instead, the device undergoes a single stability transition, after which it vibrates about a pre-stressed, geometrically nonlinear equilibrium configuration. The apparent "mode changes" observed in the frequency response and displacement fields therefore reflect shifts in the dominant vibration mode along this equilibrium path, consistent with classical plate stability theory when imperfections are present.

3.3.4. Parametric response

We then investigate the parametric response of the RR-based IPUT for a range of internal stress values (from 0 Pa to 1 GPa similar to the case of MZI-based IPUT discussed in the previous section) and frequencies (1 Hz to 8 MHz).

The variation in the resonance frequency as a function of the applied internal stress is shown in Fig. 13(a), where the actual resonance frequency of the device $f_c = 0.77$ MHz and the internal stress $\sigma_0 = -425$ MPa are marked. Similar to the case of MZI, the parametric response is separated into three zones based on the dominant mode shape of the IPUT. In the first zone spanning from $\sigma = 0$ Pa to $\sigma = 130$ MPa and f ranging from 0.615 MHz to 0.185 MHz, the frequency continuously decreases with increasing internal stress and the IPUT vibrates in its fundamental mode as shown in Fig. 13(d). At approximately 140 MPa, the flat equilibrium

Table 2
Comparison of buckling analysis with the dynamic response of the RR-based IPUT. Similarly to the MZI case, the buckling and dynamic modes are very similar for corresponding critical loads. The displacements are also normalized for better visualization. The surface displacement ranges for the first mode from 0 pm to 50 pm, the second mode from 0 pm to 15 pm, and the third mode from 0 pm to 70 pm.

Mode	Critical Load σ_{cr} (MPa)	Dominant frequency (MHz)	Normalized buckling mode	Normalized dynamic mode
1	142	0.19	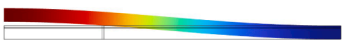	
2	469	0.32		
3	962	0.2		
			0	1

configuration loses stability and the vibration response transitions to oscillation about a post-buckled equilibrium configuration (see Fig. 13(e)), accompanied by a sharp increase in resonance frequency (2.85 MHz). As the waveguide's dimensions are much smaller than those of the plate, we can assume that the plate's dynamic behavior is not influenced by the waveguide itself. Hence, the analytical expression for the lowest critical buckling load of a clamped circular plate (Eq. (2)) provides a useful reference (141 MPa) for interpreting the numerical transition point. It is very close to the prediction of the model (140 MPa). The post-buckling behavior of the RR-based IPUT is similar to the MZI-based IPUT, i.e., frequency decreases with the increase in the internal stress until a higher buckling eigenvalue is reached ($\sigma_2 = 460$ MPa), where the dominant vibration mode changes again (as shown in Fig. 13(f)), and then the trend continues. The maximum difference in the resonance frequencies for the complete internal stress range is 36 times, which is higher than the MZI-based IPUT case (11.7 times). The calculated RTF is presented in Fig. 13(b), where the actual RTF of the device $\mathrm{RTF}_c = \mathrm{RTF}_c = 0.066$ pm/Pa as well as the corresponding internal stress σ_t are marked. Since the internal stress value is close to a peak (near the end of the second critical load), the RTF has a high value. The RTF increases with internal stress up to the vicinity of the lowest critical buckling load, after which the transition to a post-buckled equilibrium configuration leads to a sharp change in RTF; then the same trend continues. The largest variation of the RTF is 7800, which includes the influence of the frequency, and thus the RTF is updated by multiplying it by F_s, as shown in Fig. 13(c). Here, the trend stays the same as the RTF plot Fig. (13(b)) while the ranges are significantly decreased (from 7800 to 1225). However, there still exists a three orders of difference between the highest and lowest RTF values, which is significant for the IPUTs' performance. As in the MZI-based IPUT, only the lowest critical buckling load corresponds to a physical loss of stability of the flat configuration; higher critical stresses identified in the analysis represent eigenvalue-based reference points for changes in the vibration response rather than additional buckling events.

4. Discussions

From the parametric study of plate-based IPUTs with different geometries, we can state that the internal stress plays a crucial role in the dynamic behavior of the IPUT. For the same IPUT device, within the possible internal stress limits, the resonance frequency and RTF can experience drastic changes. The resonance frequency may vary by more than one order of magnitude as the equilibrium configuration and dominant vibration mode change with internal stress. This can drastically alter the performance of the device from its intended purpose if internal stress is not considered during the design stage. In general, the bow experienced by the wafer (after the oxidation process) is used to estimate the internal stress. The internal stress may therefore be considered a design parameter that must be accounted for during fabrication and layout, rather than an actively tunable quantity. While in electrostatically actuated devices such as cMUTs and pMUTs the effective prestress can be modified via bias voltage, in IPUTs the stress state is primarily set during fabrication and must therefore be accommodated through design. Noteworthy, the position of the optical waveguide on the plate should be accurately determined based on the internal stress and displacement profile of the IPUT so that the waveguide's radial deflection is maximum. Otherwise, the RTF will be much lower than the designed value. For instance, if the waveguide location is designed by assuming the fundamental vibration mode for the IPUT, while it operates in the second mode due to internal stress, the waveguide might end up in a low radial displacement position (on the plate), limiting the IPUT's performance. From the comparison between MZI and RR based IPUTs, it is evident that the location of the waveguide, distance from the neutral plane

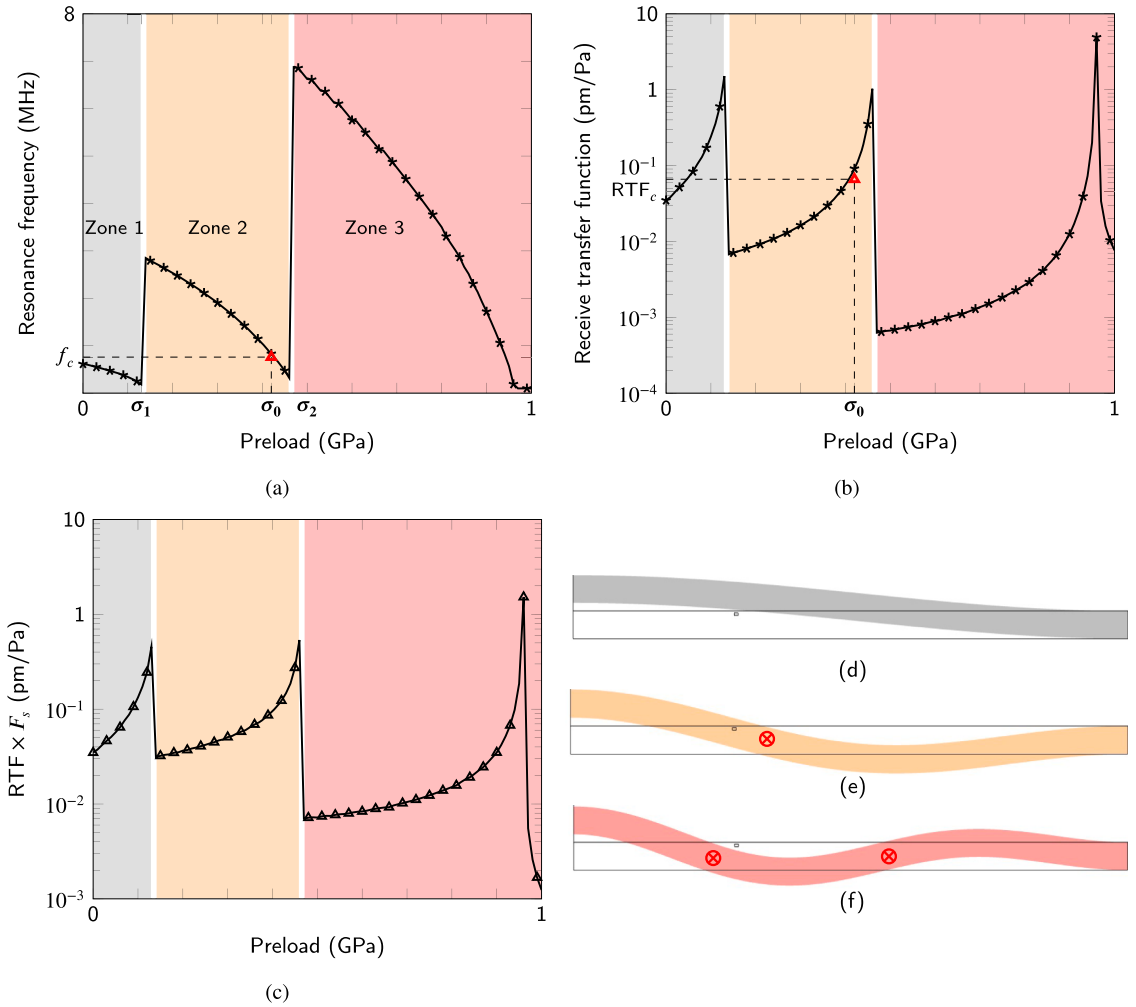

Fig. 13. Parametric response of the RR-based IPUT: (a) Resonance frequency variation with internal stress from 0 to1 GPa where the lowest critical buckling load $\sigma_1 = -140$ MPa and a higher buckling eigenvalue $\sigma_2 = -460$ MPa are marked. The plot is separated into three zones based on changes in the dominant vibration mode of the prestressed equilibrium configuration. There are sharp discontinuities between each zone, indicating the transition in the dominant vibration mode. The internal stress experienced by the IPUT ($\sigma_t = -425$ MPa) and the corresponding resonance frequency ($f_c = 0.77$ MHz) obtained from the literature are also marked here. (b) The variation of RTF with the internal stress, where sudden increases in RTF values close to critical loads are visible. The internal stress σ_t and corresponding RTF (RTF$_c$ = 0.066 pm/Pa also from the literature) are marked in the plot. (c) The variation of the product of RTF with the frequency ratio (F_s) is plotted for the same range of internal stress. (d), (e) and (f), respectively, are displacement profiles of the RR-based IPUT for different frequencies and internal stresses: (d) 0.445 MHz and −70 MPa IPUT's behavior in Zone 1 vibrating in its fundamental mode. (e) 0.78 MHz and −425 MPa IPUT's behavior in the actual condition, which is in Zone 2, where its deformation pattern is similar to a second vibration mode with the presence of a node (red cross). (f) 3.5 MHz and −800 MPa operating in Zone 3 after crossing the second critical load, where the IPUT's displacement profile is equivalent to the third vibration mode with two nodes. (For interpretation of the references to colour in this figure legend, the reader is referred to the web version of this article.)

and most importantly, the dominating vibration mode plays crucial roles in the resulting sensitivity and operating frequency. In the case of MZI, the waveguides were located at the optimum position of the plate (correspond to region of large radial displacement of the plate) and away from the neutral plane, the variation in the sensitivity due to the internal stress was not as severe as in the case of the RR where both parameters were not at optimum. Additionally, regions near the sharp transitions (refer to Figs. 9 and 13) should be avoided in practice, as small variations in fabrication-induced stress can lead to disproportionately large changes in resonance frequency and RTF. as they are unstable regions due to the fabrication margins. In other words, close to these peaks, small variations in the fabrication process can lead to substantial changes in the performance parameters. For instance, an increase in the plate thickness by 5 % could increase the resonance frequency by the same amount (assuming fundamental mode behavior with the same internal stress), which can be close to the peaks leading to completely different dynamic response. Overall, the results highlight that the observed discontinuities in frequency and RTF arise from changes in the equilibrium configuration and dominant vibration

mode, rather than from repeated physical buckling events, reinforcing the importance of interpreting prestressed plate dynamics within a nonlinear vibration framework.

5. Summary and conclusions

In this work, we numerically investigated the influence of fabrication-induced internal stress on the dynamic behavior of integrated photonic ultrasound transducers (IPUTs). Finite element models were developed in which the residual stress in the oxide layer was incorporated through a geometrically nonlinear formulation. The numerical model was validated by comparison with experimental measurements from our previous work and with results reported in the literature. Incorporating realistic internal stress values significantly improved the agreement between the simulated and measured resonance frequencies and receive transfer functions (RTFs).

A systematic parametric study was then conducted by varying the internal stress over a wide compressive range. The results show that increasing compressive stress reduces the effective structural stiffness of the plate, leading to a decrease in the fundamental resonance frequency. As the compressive stress approaches the critical level associated with elastic instability, the frequency reaches a minimum and the vibration characteristics change due to a modification of the equilibrium configuration and mode shapes. In practical devices, fabrication imperfections smooth the bifurcation behavior, resulting in a finite minimum frequency rather than a vanishing value predicted for an ideal structure.

The analysis reveals that internal stress not only shifts the resonance frequency but can also significantly alter the spatial deformation patterns of the vibrating plate, which in turn affects the optical sensitivity of the device. These stress-induced modifications lead to distinct operational regimes in the frequency-stress response and corresponding variations in the receive transfer function.

Based on the numerical and experimental observations, the following conclusions can be drawn:

- The internal stress developed in thin-film structures, such as oxide or nitride, plays a dominant role in determining the dynamic response of IPUTs and must be incorporated in the design and simulation stages for accurate prediction of device performance.
- The proposed modeling framework can be extended to other membrane/plate-based acoustic sensors where residual stress significantly influences the vibration characteristics.
- Internal stress can be used as a design parameter to tailor the resonance frequency and sensitivity of the transducer by modifying the effective stiffness and vibration mode shapes of the plate.
- Care must be taken to avoid operating conditions near the critical instability regime, since fabrication tolerances may introduce small variations in residual stress that can significantly alter the resonance frequency and receive transfer function.

Overall, the present study highlights the critical role of residual stress in determining the vibration behavior of thin plates in photonic ultrasound transducers. By tuning the process parameters (e.g., furnace temperature during thermal oxidation), the internal stress may be controlled. Additionally, the resulting stress can be measured by using the wafer bow (as mentioned in the discussions), so that it can be used for improving the designs.

CRediT authorship contribution statement

Sabiju Valiya Valappil: Writing - original draft, Visualization, Validation, Software, Resources, Methodology, Investigation, Formal analysis, Conceptualization; **Martin Verweij:** Writing - review & editing, Supervision, Resources, Project administration, Funding acquisition; **Peter Harmsma:** Writing - review & editing, Supervision, Investigation, Funding acquisition; **Maurits van der Heiden:** Writing - review & editing, Supervision, Project administration, Methodology, Funding acquisition; **Paul van Neer:** Writing - review & editing, Supervision, Resources, Investigation, Funding acquisition.

Data availability

Data will be made available on request.

Declaration of competing interest

The authors declare that they have no known competing financial interests or personal relationships that could have appeared to influence the work reported in this paper.

Acknowledgment

The authors greatly appreciate the support from the funding partner Nederlandse Organisatie voor Wetenschappelijk Onderzoek (NWO) for the grant entitled “Opto acoustic sensor and ultrasonic microbubbles for dosimetry in proton therapy” with the grant number NWA-1160.18.095.

References

[1] B.W. Drinkwater, P.D. Wilcox, Ultrasonic arrays for non-destructive evaluation: a review, NDT Int. 39 (7) (2006) 525–541. https://doi.org/10.1016/j.ndteint.2006.03.006

[2] A. Carovac, F. Smajlovic, D. Junuzovic, Application of ultrasound in medicine, Acta Inform. Med. 19 (3) (2011) 168–171.

[3] M.L. Sanderson, H. Yeung, Guidelines for the use of ultrasonic non-invasive metering techniques, Flow Meas. Instrum. 13 (4) (2002) 125–142. https://doi.org/10.1016/S0955-5986(02)00043-2

[4] A. Carullo, M. Parvis, An ultrasonic sensor for distance measurement in automotive applications, IEEE Sens. J. 1 (2001) 143.

[5] T.S. Awad, H.A. Moharram, O.E. Shaltout, D. Asker, M.M. Youssef, Applications of ultrasound in analysis, processing and quality control of food: a review, Food Res. Int. 48 (2) (2012) 410–427. https://doi.org/10.1016/j.foodres.2012.05.004

[6] G.M. Insight, Diagnostic ultrasound market share: statistics report, 2023–2032, 2022. https://www.gminsights.com/industry-analysis/diagnostic-ultrasound-market.

[7] M.a. Markets, Ultrasound Market by Technology, Global Forcast to 2028, 2023. https://www.marketsandmarkets.com/Market-Reports/ultrasound-market-467.{html}.

[8] J.F. Tressler, S. Alkoy, R.E. Newnham, Piezoelectric sensors and sensor materials, J. Electroceramics 2 (4) (1998) 257–272. https://doi.org/10.1023/A:1009926623551

[9] A. Rahim, J. Goyvaerts, B. Szelag, J.-M. Fedeli, P. Absil, T. Aalto, M. Harjanne, C. Littlejohns, G. Reed, G. Winzer, S. Lischke, L. Zimmermann, D. Knoll, D. Geuzebroek, A. Leinse, M. Geiselmann, M. Zervas, H. Jans, A. Stassen, C. Domínguez, P. Muñoz, D. Domenech, A.L. Giesecke, M.C. Lemme, R. Baets, Open-access silicon photonics platforms in Europe, IEEE J. Sel. Top. Quantum Electron. 25 (5) (2019) 1–18. https://doi.org/10.1109/JSTQE.2019.2915949

[10] J. Jung, W. Lee, W. Kang, E. Shin, J. Ryu, H. Choi, Review of piezoelectric micromachined ultrasonic transducers and their applications, J. Micromech. Microeng. 27 (11) (2017) 113001. https://doi.org/10.1088/1361-6439/aa851b

[11] A.K. Ilkhechi, C. Ceroici, Z. Li, R. Zemp, Transparent capacitive micromachined ultrasonic transducer (CMUT) arrays for real-time photoacoustic applications, Opt. Express 28 (9) (2020) 13750–13760. https://doi.org/10.1364/OE.390612

[12] S. Basiri-Esfahani, A. Armin, S. Forstner, W.P. Bowen, Precision ultrasound sensing on a chip, Nat. Commun. 10 (1) (2019) 132. https://doi.org/10.1038/s41467-018-08038-4

[13] S. Franssila, Introduction to Microfabrication, John Wiley & Sons, 2010.

[14] B. Ouyang, Y. Li, M. Kruidhof, R. Horsten, K.W.A. van Dongen, J. Caro, On-chip silicon Mach–Zehnder interferometer sensor for ultrasound detection, Opt. Lett. 44 (8) (2019) 1928–1931. https://doi.org/10.1364/OL.44.001928

[15] L.-C. Chen, Review of preparation and optoelectronic characteristics of Cu2O-based solar cells with nanostructure, Mater. Sci. Semicond. Process. 16 (5) (2013) 1172–1185. Advanced Oxides for Electronics, https://doi.org/10.1016/j.mssp.2012.12.028

[16] J.T. Wright, D.J. Carbaugh, M.E. Haggerty, A.L. Richard, D.C. Ingram, S. Kaya, W.M. Jadwisienczak, F. Rahman, Thermal oxidation of silicon in a residual oxygen atmosphere–the RESOX process–for self-limiting growth of thin silicon dioxide films, Semicond. Sci. Technol. 31 (10) (2016) 105007. https://doi.org/10.1088/0268-1242/31/10/105007

[17] E. Kobeda, E.A. Irene, SiO2 film stress distribution during thermal oxidation of Si, J. Vac. Sci. Technol. B Microelectron. Process. Phenom. 6 (2) (1988) 574–578. https://doi.org/10.1116/1.584402

[18] M. Ohring, Materials Science of Thin Films: Depositon and Structure, Academic press, 2002.

[19] S. Kamiya, J. Kuypers, A. Trautmann, P. Ruther, O. Paul, Annealing temperature dependent strength of polysilicon measured using a novel tensile test structure, in: 17th IEEE International Conference on Micro Electro Mechanical Systems. Maastricht MEMS 2004 Technical Digest, 2004, pp. 185–188. https://doi.org/10.1109/MEMS.2004.1290553

[20] S. Dutta, A. Pandey, Overview of residual stress in MEMS structures: its origin, measurement, and control, J. Mater. Sci. Mater. Electron. 32 (6) (2021) 6705–6741. https://doi.org/10.1007/s10854-021-05405-8

[21] G.G. Yaralioglu, A.S. Ergun, B. Bayram, T. Marentis, B.T. Khuri-Yakub, Residual stress and Young's modulus measurement of capacitive micromachined ultrasonic transducer membranes, in: 2001 IEEE Ultrasonics Symposium. Proceedings. an International Symposium (Cat. No.01CH37263), 2, 2001, pp. 953–956 vol.2. https://doi.org/10.1109/ULTSYM.2001.991877

[22] P. Xu, T. Yu, F. Yu, Investigation of residual stress influence on CMUT in standard CMOS process, in: 2011 International Conference on Electric Information and Control Engineering, 2011, pp. 495–498. https://doi.org/10.1109/ICEICE.2011.5777283

[23] V. Walter, G. Bourbon, P. Le Moal, Residual stress in capacitive micromachined ultrasonic transducers fabricated with anodic bonding using SOI wafer, Procedia Eng. 87 (2014) 883–886. EUROSENSORS 2014, the 28th European Conference on Solid-State Transducers, https://doi.org/10.1016/j.proeng.2014.11.295

[24] G. Ross, H. Dong, C.B. Karuthedath, A.T. Sebastian, T. Pensala, M. Paulasto-Kröckel, The impact of residual stress on resonating piezoelectric devices, Mater. Des. 196 (2020) 109126. https://doi.org/10.1016/j.matdes.2020.109126

[25] A. Dangi, R. Pratap, System level modeling and design maps of PMUTs with residual stresses, Sens. Actuators A Phys. 262 (2017) 18–28. https://doi.org/10.1016/j.sna.2017.05.006

[26] V. Rochus, R. Jansen, J. Goyvaerts, P. Neutens, J. O'Callaghan, X. Rottenberg, Fast analytical model of MZI micro-opto-mechanical pressure sensor, J. Micromech. Microeng. 28 (6) (2018) 064003. https://doi.org/10.1088/1361-6439/aab461

[27] W.J. Westerveld, S.M. Leinders, P.L. M.J. van Neer, H.P. Urbach, N.d. Jong, M.D. Verweij, X. Rottenberg, V. Rochus, Optical micro-machined ultrasound sensors with a silicon photonic resonator in a buckled acoustical membrane, in: 2019 20th International Conference on Thermal, Mechanical and Multi-Physics Simulation and Experiments in Microelectronics and Microsystems (EuroSimE), 2019, pp. 1–7. https://doi.org/10.1109/EuroSimE.2019.8724528

[28] V. Rochus, R. Jansen, R. Haouari, B. Figeys, V. Mukund, F. Verhaegen, J. Goyvaerts, P. Neutens, J. O'. Callaghan, A. Stassen, S. Lenci, X. Rottenberg, Modelling and design of micro-opto-mechanical pressure sensors in the presence of residual stresses, in: 2017 18th International Conference on Thermal, Mechanical and Multi-Physics Simulation and Experiments in Microelectronics and Microsystems (EuroSimE), 2017, pp. 1–5. https://doi.org/10.1109/EuroSimE.2017.7926285

[29] R. Zhang, C. Ti, M.I. Davanço, Y. Ren, V. Aksyuk, Y. Liu, K. Srinivasan, Integrated tuning fork nanocavity optomechanical transducers with high fMQM product and stress-engineered frequency tuning, Appl. Phys. Lett. 107 (13) (2015) 131110. https://doi.org/10.1063/1.4932201

[30] Analytical modeling of an implantable opto-mechanical pressure sensor to study long term drift, vol. ASME 2020 29th Conference on Information Storage and Processing Systems Information Storage and Processing Systems, 2020. https://doi.org/10.1115/ISPS2020-1945

[31] K.F. Wang, B.L. Wang, Approximate and explicit expression of optical forces and pull-in instability of a silicon nano-optomechanical device, Nanotechnology 30 (8) (2019) 085502. https://doi.org/10.1088/1361-6528/aaf5b5

[32] M.L. Reed, G.K. Fedder, 2 - Photolithographic Microfabrication, in: T. Fukuda, W. Menz (Eds.), Micro Mechanical Systems, 6 of *Handbook of Sensors and Actuators*, Elsevier Science B.V., 1998, pp. 13–61. https://doi.org/10.1016/S1386-2766(98)80003-0

[33] J.A. Thornton, D.W. Hoffman, Stress-related effects in thin films, Thin Solid Films 171 (1) (1989) 5–31.

[34] Y. Okada, Y. Tokumaru, Precise determination of lattice parameter and thermal expansion coefficient of silicon between 300 and 1500 K, J. Appl. Phys. 56 (2) (1984) 314–320. https://doi.org/10.1063/1.333965

[35] B. El-Kareh, L.N. Hutter, Fundamentals of Semiconductor Processing Technology, Springer Science & Business Media, 2012.

[36] M. Huff, Review paper: residual stresses in deposited thin-film material layers for micro- and nano-systems manufacturing, Micromachines 13 (12) (2022). https://doi.org/10.3390/mi13122084

[37] F. Bloom, D. Coffin, Handbook of Thin Plate Buckling and Postbuckling, CRC Press, 2000.

[38] S.P. Timoshenko, J.M. Gere, Theory of Elastic Stability, Courier Corporation, 2012.

[39] L.S. Cheo, E.L. Reiss, Secondary buckling of circular plates, SIAM J. Appl. Math. 26 (3) (1974) 490–495. https://doi.org/10.1137/0126046

[40] A. Bedford, D.S. Drumheller, Introduction to Elastic Wave Propagation, Springer Nature, 2023.

[41] A.D. Pierce, Acoustics: An Introduction to its Physical Principles and Applications, Springer, 2019.
[42] G. Bao, Y. Gao, P. Li, Time-domain analysis of an acoustic–elastic interaction problem, Arch. Ration. Mech. Anal. 229 (2) (2018) 835–884. https://doi.org/10.1007/s00205-018-1228-2
[43] J. Bonet, R.D. Wood, Nonlinear Continuum Mechanics for Finite Element Analysis, Cambridge university press, 1997.
[44] J.N. Reddy, An Introduction to Continuum Mechanics, Cambridge university press, 2013.
[45] S.V. Valappil, P. Harmsma, M. van der Heiden, M. Verweij, P. van Neer, Semi-analytical modeling of receive transfer function and thermal noise of integrated photonic ultrasound transducers, Appl. Math. Model. (2025) 116381. https://doi.org/10.1016/j.apm.2025.116381
[46] S.V. Valappil, M. Verweij, P. Harmsma, M. van der Heiden, A.M. Gerritsma, R. Altmann, P. van Neer, Sensitive integrated photonic transducer with predictive modeling for underwater ultrasound sensing, Opt. Express 33 (17) (2025) 35460–35478. https://doi.org/10.1364/OE.571595
[47] S.M. Leinders, W.J. Westerveld, J. Pozo, P.L. M.J. van Neer, B. Snyder, P. O'Brien, H.P. Urbach, N. de Jong, M.D. Verweij, A sensitive optical micro-machined ultrasound sensor (OMUS) based on a silicon photonic ring resonator on an acoustical membrane, Sci. Rep. 5 (1) (2015) 14328. https://doi.org/10.1038/srep14328